Enhancement of the hydrogen release of Mg(BH4)2 by concomitant effects of nano-confinement and catalysis

Damien Clémençon, Carine Davoisne, Jean-Noël Chotard, Raphaël Janot

Enhancement of the hydrogen release of $Mg(BH_4)_2$ by concomitant effects of nano-confinement and catalysis

D. Clémençon, C. Davoisne, J-N. Chotard and R. Janot*

Laboratoire de Réactivité et Chimie des Solides (LRCS), CNRS UMR 7314,

Université de Picardie Jules Verne, 33 Rue Saint Leu, 80039 Amiens Cedex, FRANCE

* Corresponding author. Email: raphael.janot@u-picardie.fr. Tel: +(33)3.22.82.57.77

Abstract

Magnesium borohydride, $Mg(BH_4)_2$, is an interesting material for hydrogen storage due to its high hydrogen content (14.9 wt.% of H_2). Unfortunately, a temperature of at least 350°C is needed for releasing its hydrogen and the rehydrogenation process is only feasible under harsh conditions (950 bar H_2 and 300°C). In order to improve the performances of this compound, we analyze in this study the concomitant effects of nano-confinement into mesoporous carbons and addition of Ni-Pt catalysts. This study uses different characterization tools to determine the effects of both nano-confinement and catalysts onto the pathway of decomposition. Usually, bulk $Mg(BH_4)_2$ decomposes in several steps passing through intermediate species for which activation energies are high. In this study, we show that the confinement and catalyst addition on $Mg(BH_4)_2$ result in a single step of hydrogen release and an activation energy below that of the bulk material with a value of 178 ± 14 $kJ.mol^{-1}$ as determined by the Kissinger's method. Interestingly, the hydrogen release is fully completed, i.e. 8 H atoms per $Mg(BH_4)_2$ formula unit are released, in less than 2 hours at 350°C.

Keywords: Magnesium borohydride; Hydrogen storage; Activation energy; Nano-catalyst; Nano-confinement

1. Introduction

Hydrogen possesses a high potential as an energy vector [1-2] thanks to its high energy density, a renewable production [3-4] and a clean consumption, but the low density of hydrogen gas under normal temperature and pressure conditions limits its development. There are different ways to store hydrogen: as pressurized bottles (700 bar) [5] or eventually cryogenic containers (20 K) [6] or even both at the same time using hybrid containers [7], but these techniques are associated with energy losses and have to pass rigorous safety tests to be used in daily life. Finally, these storage systems are quite expensive. An alternative can be the solid storage of hydrogen using metals or complex hydrides [8-9]. Among the complex hydrides with the highest gravimetric hydrogen contents, we can cite $Be(BH_4)_2$ [10], $LiBH_4$ [11-12] and $Al(BH_4)_3$ [13] with a hydrogen content of 20.8 wt.%, 18.5 wt.% and 16.9 wt.%, respectively [14]. These compounds are interesting due to their high gravimetric and volumetric capacities and they could be used to supply energy for mobile applications. However, some issues limit their use as the toxicity (Be), slow kinetics, high activation energy and high temperature of decomposition in most cases [15]. We can also cite a more specific problem to borohydrides, which is their tendency to release diborane (B_2H_6), which is a strong poison for fuel cells but also for human beings. For these reasons, most of complex hydrides cannot be used today in real applications.

One of the most promising and studied complex hydride so far is $Mg(BH_4)_2$, which shows an interesting behavior from both applicative and fundamental points of view. First, this compound exists as several polymorphs, five of them are stable under ambient conditions and another 6th polymorph is metastable (ε phase). All of these polymorphs have different volumetric hydrogen contents ranging from 82 g $H_2.L^{-1}$ [16] for porous γ-$Mg(BH_4)_2$ to 147 g $H_2.L^{-1}$ for the high density δ-$Mg(BH_4)_2$ phase obtained under high pressures, this latter value being one of the highest reported for complex hydrides. Regarding the gravimetric capacity, it is also one of the highest with 14.9 wt.% of hydrogen [17] for $Mg(BH_4)_2$. The enthalpy of the hydrogen release is theoretically suitable for reversible hydrogen storage near ambient conditions, as predicted by several modeling methods [18-20] with calculated ΔH_{298K} of -38 kJ.mol^{-1} H_2 and -44 kJ.mol^{-1} H_2 for reactions 1 and 2, respectively. These results are in a good agreement with the observations made by Nakamori *et al*. [8] concerning the relationship between the energy of decomposition and the cations

electronegativity: more is the cation electronegative, less is the borohydride stable. The enthalpy value determined for $Mg(BH_4)_2$ could lead to the release of one bar H_2 in a single step at temperatures around 20-75°C [20].

But, experimentally, it was shown by many authors [21-27] that the reaction occurs around 300°C in a three steps process with an activation energy as high as 311 ± 20 $kJ.mol^{-1}$ as determined by Fichtner *et al*. [28]. The formation of $MgB_{12}H_{12}$ as a stable intermediate is often observed, thanks to ^{11}B NMR spectroscopy, and is responsible for the high activation energy of the desorption process. Finally, the reaction is most of the time incomplete at 350°C leading to the formation of MgH_2 + 2 B [9] (cf. reaction 2). The total desorption of hydrogen is only feasible at temperatures above 400°C with the formation of MgB_2 at the end of the reaction (cf. reaction 1).

$$\mathbf{Mg(BH_4)_2 \rightarrow MgB_2 + 4\ H_2} \quad \mathbf{(1)}$$

$$\mathbf{Mg(BH_4)_2 \rightarrow MgH_2 + 2\ B + 3\ H_2} \quad \mathbf{(2)}$$

In this study, we focus mainly on the decrease of the activation energy of the decomposition reaction of $Mg(BH_4)_2$ and the formation of MgB_2 nanoparticles at the end of the reaction. Several studies were made to decrease the activation energy and the decomposition temperature of $Mg(BH_4)_2$, namely the nano-confinement of $Mg(BH_4)_2$ [28] and/or mixing with some additives [29]. Many compounds were investigated as additives for the decomposition of $Mg(BH_4)_2$, mainly transition metal-based additives such as $TiCl_3$, TiO_2, $NbCl_5$, $CoCl_2$, Ni and NiO, allowing a decrease in the decomposition temperature of $Mg(BH_4)_2$ but the rehydrogenation process was rarely studied. The nano-confinement has also shown an interesting effect on $Mg(BH_4)_2$ decomposition: for example a lower activation energy by confining $Mg(BH_4)_2$ into a disorganized mesoporous carbon [28]. Magnesium borohydride was also confined into silica aerogels by Rueda *et al* [30], where it has been demonstrated that the SiO_2 particles could lower the temperature of decomposition by 60°C and change the decomposition pathway of $Mg(BH_4)_2$. Some research groups also mixed $Mg(BH_4)_2$ with others hydrides, especially alanates such as $NaAlH_4$ [31] or $LiAlH_4$ [32], leading to a metathesis reaction and thus to the formation of $Mg(AlH_4)_2$ and $NaBH_4$ or $LiBH_4$, respectively. This led to a complete change of reaction path, a strong decrease of the

decomposition temperatures and, a partial rehydrogenation of the decomposition products was possible.

So far, very few studies deal with the combined effects of nano-confinement and catalyst on $Mg(BH_4)_2$. Only, Wahab et al. studied the effects of Ni catalysts embedded into porous carbons [33-34] and they were able to decompose $Mg(BH_4)_2$ at lower temperatures with an activation energy about twice lower than that of bulk $Mg(BH_4)_2$. Based on our experiences with $LiBH_4$ about nano-confinement [35-36] and additives [37-38], we apply our previous works to $Mg(BH_4)_2$ in order to decrease the activation energy and to promote the MgB_2 formation. Especially, the use of core-shell Ni-Pt nanoparticles as catalysts is carried on for the first time in the case of the $Mg(BH_4)_2$ thermal decomposition. Core-shell nanoparticles composed of a non-noble metal core (Ni) and a noble metal shell (Pt) are of great significance in many areas including catalysis, optical detection, and magnetic separation. Although the Ni@Pt nanoparticles have a much reduced content of Pt, they are known to exhibit significantly enhanced catalytic activity as compared to pure Pt particles [38-39].

The synthesis of $Mg(BH_4)_2$ and especially the incipient impregnation method used to obtain the carbon-supported $Mg(BH_4)_2$ nanoparticles are described in this paper. Finally, the concomitant effects of nano-confinement and Ni-Pt core-shell nanocatalysts on the hydrogen desorption performances are presented.

2. Experimental

2.1. Materials

Mesoporous carbon (Sigma-Aldrich), nickel (II) sulfate heptahydrate ($NiSO_4$-$7H_2O$, Acros Organics, 99.999 %), potassium hexachloro-platinate monohydrate (K_2PtCl_6-$1H_2O$, Sigma-Aldrich, 98 %), cetyl-trimethyl-ammonium bromide (CTAB, Sigma-Aldrich, 99 %), diethyl ether (Acros Organics, 99 %), magnesium chloride ($MgCl_2$, Sigma-Aldrich, 98 %) and sodium borohydride ($NaBH_4$, Sigma-Aldrich, 98 %) were used as reactants. All of them except the diethyl ether (dried on molecular sieves before use) were used as received without any purification.

2.2. Synthesis of $Mg(BH_4)_2$

For the synthesis of magnesium borohydride $Mg(BH_4)_2$, 2.8 g of sodium borohydride ($NaBH_4$) and 3.53 g of magnesium chloride ($MgCl_2$) were mixed into 40 mL of diethyl ether (< 20 ppm of water) in a steel ball-milling jar (45 mL) with a balls (10 mm diameter) to powder weights ratio of 5:1. The milling was performed under inert atmosphere (Ar) for 12 h at 100 rpm using a Retsch PM100 planetary ball-milling apparatus. The synthesis reaction is as follows:

$$\mathbf{MgCl_2 + 2\ NaBH_4 \rightarrow Mg(BH_4)_2 + 2\ NaCl} \qquad \mathbf{(3)}$$

This synthesis method is interesting due to the use of $NaBH_4$ instead of $LiBH_4$, the NaCl formed as by-product being easier to separate from $Mg(BH_4)_2$, thanks to an extremely low solubility in diethyl ether compared to LiCl. Then, the mixture was filtrated using a Büchner in a glovebox (< 1 ppm H_2O, < 1 ppm O_2) under argon to remove the reactants leftover as well as NaCl. The resulting ether solution containing only $Mg(BH_4)_2$ is kept under inert atmosphere for further uses. We have to note that the concentration of the resulting $Mg(BH_4)_2$ solution varies rapidly due to the low boiling point of diethyl ether (34.6°C) and, thus, its concentration must be determined just before the impregnation into the porous carbon. The concentration of the solution is usually determined by drying a known volume of solution at 150°C under dynamic vacuum and weighing the solid residue.

2.3. Synthesis of the metal catalysts

The carbon-supported catalyst nanoparticles were obtained by reduction of two metallic precursors. First, the mesoporous carbon, $NiSO_4$ heptahydrate, K_2PtCl_6 monohydrate and CTAB were mixed together. CTAB is used here as a surfactant to avoid the growth of metallic nanoparticles. The mixture was heated at 50°C for 1 h to completely dissolve the surfactant and K_2PtCl_6. Then the solution was ultra-sonicated until no more carbon aggregates were present at the bottom of the flask. The metallic salts were then reduced by addition of a hydrazine:water solution

(50:50 by volume) and 0.5 g of $NaBH_4$. The solution was stirred for a few hours until the gas release stopped. This gas release can be fastened by slightly heating the solution since the reduction occurs quickly and the gas release is due to the decomposition of hydrazine in contact with the newly formed nanoparticles. The solution was then filtrated and the Ni-Pt@C sample was firstly dried in an oven at 175°C under dynamical vacuum and finally heat-treated at 5°C/min in a tubular furnace in a quartz tube with a flow of Ar/H_2 at 800°C for 1 h. The sample was characterized by Transmission Electronic Microscopy (TEM) and related spectroscopic techniques in order to determine the dispersion, size, type and oxidation state of the metallic catalysts formed inside the carbon matrix.

2.4. Infiltration of $Mg(BH_4)_2$ into Ni-Pt@C

The carbon containing the catalyst nanoparticles was then impregnated by incipient wetness method using the procedure reported elsewhere [28]: this technique allows a good control over the quantity of magnesium borohydride nucleated into the carbon. Here, 0.5 g of Ni-Pt@C was impregnated using 1 mL of $Mg(BH_4)_2$ (1 M in diethyl ether) and the sample was dried at 70°C for 15 min then 150°C for 30 min in a drying furnace (Büchi B-585). Finally, the sample was heat treated at 200°C for 12 h under vacuum for the full removal of the ether. This process was done several times until the sample reached a loading of 30 wt.% of magnesium borohydride.

2.5. Characterization tools

The porosity of the mesoporous carbons was characterized by N_2 adsorption-desorption at 77 K using a Micromeritics ASAP 2020 analyzer. Specific surface areas and pore size/volume distribution were calculated using the BET (Brunauer-Emmet-Teller) and BJH (Barrett-Joyner-Halenda) formalisms, respectively. The carbon samples were outgassed under vacuum at 300°C for 6 h before the N_2 exposure.

The samples containing $Mg(BH_4)_2$ were characterized by X-ray diffraction (XRD) on a Bruker D8 Advance diffractometer (Cu radiation, λ = 1.5418 Å) equipped with a cryo-furnace loaded in the glovebox to avoid any contact with oxygen/moisture. The cryo-furnace allowed the

analysis of the samples from 20 to 450°C and the identification of the different phases formed during the thermal decomposition.

The thermal analysis of the samples were done both by DSC calorimetry and thermogravimetric analysis (TGA-MS). For DSC (Differential Scanning Calorimetry), a Netzsch DSC 204 F1 apparatus was used with aluminum crucibles sealed in the glove box. In order to avoid crucible deformation due to gas release, the lids of the crucibles were holed just prior to the heating. Thermogravimetric analyses (Netzsch STA 449 C coupled to a QMS 403C mass spectrometer) were performed at different heating rates using alumina crucibles. The activation energy of the decomposition of our samples was calculated using the Kissinger method from the curves of hydrogen emission (m/z = 2) recorded by mass spectroscopy at different hating rates (from 2 to 15°C/min).

Transmission Electron Microscopy (TEM) was used to look at the size and dispersion of the catalysts nanoparticles into the carbon matrix. The powders were deposited on copper grids coated with a Lacey carbon film. The sensitive samples were prepared in glove box under argon atmosphere and transferred to the TEM under argon flow. TEM images were recorded in the STEM-HAADF (Scanning Transmission Electron Microscopy - High Angle Annular Dark Field) mode giving a compositional information linked to the atomic number of the present elements. Energy Dispersive X-ray (EDX) and Electron Energy Loss Spectroscopy (EELS; resolution 1-1.2 eV) spectra were acquired to determine the composition and the oxidation state of the catalysts, respectively. TEM investigation was unsuccessful on $Mg(BH_4)_2$ nucleated into Ni-Pt@C due to decomposition under the electron beam and/or high vacuum. Nevertheless, TEM and the related spectroscopic techniques were performed on the sample dehydrogenated at 400°C to determine if MgB_2 was formed and to observe the evolution of the catalysts upon thermal decomposition and consequent hydrogen release. The analyses were performed using a Tecnai F20-S twin operating at 200 keV fitted with an EDX and Gatan Image Filter (GIF-EELS) Tridiem in post-column.

A PCT Pro-2000 apparatus from Hy-Energy LLC was used to determine the hydrogen yield and kinetics of the $Mg(BH_4)_2$ decomposition. First the sample (about 1 g) was loaded into the steel reactor in a glovebox (< 1 ppm O_2 and < 1 ppm H_2O) to avoid any reaction with moisture/air. Prior

starting the experiment, dead volumes were calibrated using He gas. For desorption analysis, the starting pressure was set to 0.01 bar and then the heating program was started to measure the gas release. After the decomposition is completed, the reactor was naturally cooled down. To analyze the rehydrogenation process, different hydrogen pressures up to 100 bar H_2 were applied and the temperature was increased up to 400°C.

3. Results and discussion

3.1. Textural characterization of the carbon loaded with metal nanoparticles

From adsorption-desorption isotherms of N_2 at 77 K, the specific surface area and the porous volume of the carbon matrix were determined to be 424 $m^2.g^{-1}$ and 0.43 $cm^3.g^{-1}$, respectively. The main pores size is around 8 nm. The catalyst was added to the carbon following the procedure described in experimental section with a loading of 5 wt.% of Ni-Pt particles. By STEM-HAADF (cf. Figure 1a), we can see that the catalyst particles corresponding to the white dots are homogeneously dispersed into the porous carbon. The catalyst particles size ranges from 0.5 to 4 nm with a mean size of 2 nm (cf. Figure S1 in the Supporting information). The global composition of the nanoparticles is in good agreement with the composition planned during the synthesis (90 wt.% of Ni and 10 wt.% of Pt) as verified by EDS analysis (cf. Figure S2 in the Supporting information). As shown in the inset in Figure 1a, the nanoparticles are surrounded by a layer with a size going up to 1 nm maximum for the bigger particles in agreement with a core-shell structure. Considering that the core of the particles are composed of nickel according to the EDS analyses, we can suggest that the shell is mainly composed of platinum as proposed by a previous work [38].

The oxidation state of the nanoparticles was investigated by EELS (cf. Figures 1b) and compared to published data. Figure 1b shows a characteristic spectrum of the Ni $L_{2,3}$ edge taken on a catalyst nanoparticle (red curve) in comparison with Ni metallic (green curve) and Ni in +II oxidation state (black curve). The Ni white lines are composed of a sharp asymmetric L_3 peak at 854.7 eV followed by a slight bump at 861.3 eV and a second asymmetric L_2 peak at 872.2 eV.

These white-lines shape and position are in agreement with Ni in metallic state (Figure 1b; L_3 at 855 eV, bump at 861.5 eV and L_2 at 872.4 eV). The inset of Figure 1b shows the spectra recorded at the O-K edge in the 520-580 eV energy loss region in which no contribution in the oxygen edge for the Ni-Pt particles is present as expected.

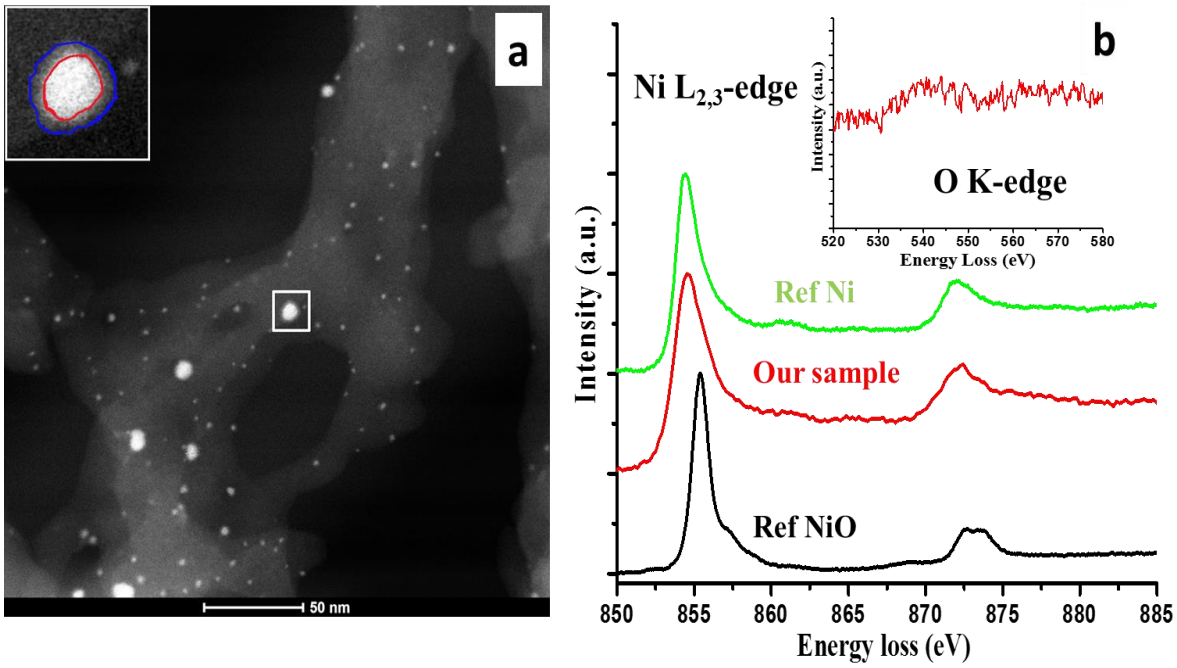

Figure 1. (**a)** STEM-HAADF image of carbon loaded with the Ni-Pt nanoparticles with in inset an enlarged view of the nanoparticles in the white square. (**b)** EELS spectra at the Ni-L2,3 edge with in inset the spectrum at the O-K edge related to our sample (Ni-Pt@C sample is plotted in red whereas Ni in green and NiO in black are used as references [40-41]).

The nickel core (schematized by the red line on inset Figure 1a) is clearly at the zero oxidation state highlighting the protective effect of the Pt shell (between the blue and red lines on inset Figure 1a). The quantity of platinum is low in the samples making its analysis difficult but, due to its high chemical stability, we assume that the platinum oxidation state is also zero. Actually, some synthesis have been done without the addition of platinum and, in these cases, nickel is quickly oxidized to form NiO nanoparticles, similarly to what has been reported in the literature [42].

3.2. Structural characterization of carbon-supported $Mg(BH_4)_2$

The sample obtained after impregnation was studied by X-ray diffraction in order to determine which $Mg(BH_4)_2$ polymorph was formed at the end of the drying heat treatment. On Figure 2, the room temperature XRD diagram for the sample Ni-Pt@C impregnated with $Mg(BH_4)_2$ is compared to those of α-$Mg(BH_4)_2$ and β-$Mg(BH_4)_2$ phases. Those phases were prepared using the same synthesis method but different heat treatments. As it can be seen on Figure 2, the polymorph obtained for the composite material after a heat treatment at 200°C is α-$Mg(BH_4)_2$. Moreover no trace of the β-$Mg(BH_4)_2$ can be identified by X-ray diffraction. The α-phase also called low temperature phase (LT) crystallizes in a hexagonal unit cell with the $P6_122$ space group. The refined unit cell parameters for our carbon-supported compound are: a=b=10.347(1) Å, c=37.103(5) Å, V=3440(1) Å^3 in good agreement with the values reported in the literature for a bulk material (a=b=10.3355 Å, c=37.0891 Å, α=β=90°, γ=120°, Z=30 and a cell volume of 3431.2 Å^3) [43].

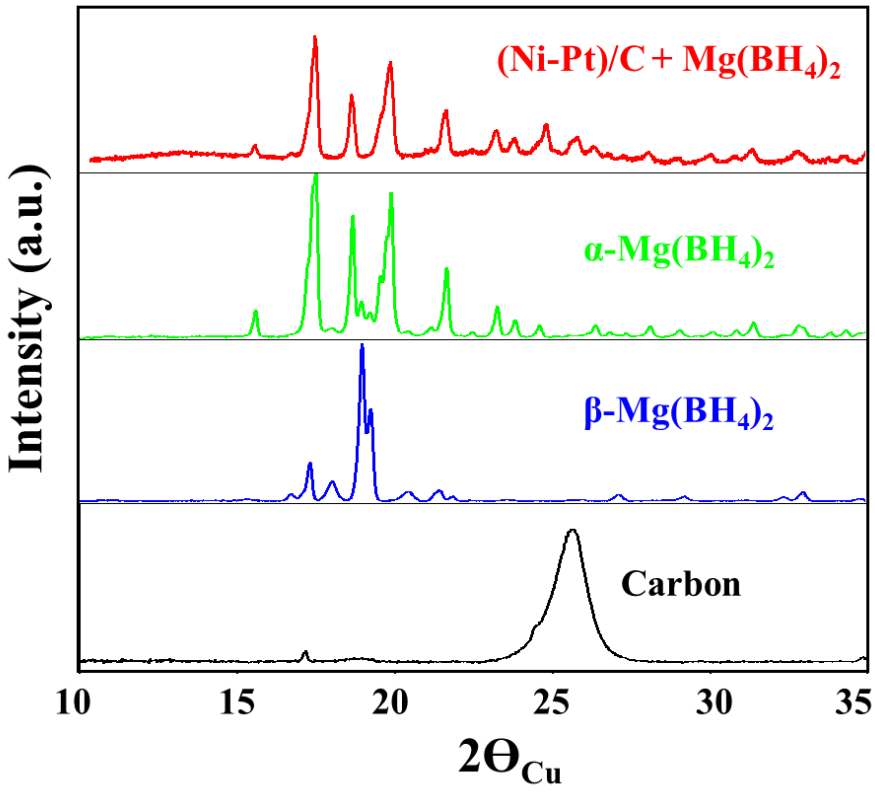

Figure 2. X-ray diagrams of $Mg(BH_4)_2$ embedded into Ni-Pt@C (Red) compared with α-$Mg(BH_4)_2$ (green), β-$Mg(BH_4)_2$ (blue) and the carbon used as confinement matrix (Black)

The phase transition of our sample was studied by X-ray diffraction equipped with a cryo-furnace. The sample was heated up to 400°C under a primary vacuum. The heating rate was set to 5°C.min^{-1} and each pattern was recorded in 1 hour. Temperature controlled XRD patterns (cf. Figure 3) clearly show the α-phase to β-phase transformation starting at 230 °C for our Ni-Pt@C/$Mg(BH_4)_2$ sample whereas, for the bulk material, the $\alpha \rightarrow \beta$ transition happens at about 190°C [44]. Thus, the confinement of $Mg(BH_4)_2$ into the carbon scaffold promotes the stability of the α-phase by more than 40°C. The β-phase also named High Temperature (HT) is orthorhombic and crystallizes in the *Fddd* space group with the following cell parameters for a bulk material: a=37.0489 Å, b=18.4919 Å, c=10.8595 Å, $\alpha=\beta=\gamma$=90°, Z=64 and a cell volume of 7439.8 Å^3 [45]. It was not possible to refine the unit cell parameters for the β-phase upon heating $Mg(BH_4)_2$ nucleated into the Ni-Pt@C matrix due to its partial decomposition resulting in bad quality diffraction data.

3.3. Dehydrogenation of Ni-Pt@C + $Mg(BH_4)_2$

As mentioned above, Figure 3 shows that the phase transition from the α-$Mg(BH_4)_2$ to β-$Mg(BH_4)_2$ begins at 230°C. The β-phase and the α-phase coexist between 230 and 250°C, and the latter phase vanishes progressively starting from 270°C and finally ends up in an amorphous material as revealed by the final XRD diagram at 300°C. In order to characterize the hydrogen release, temperature controlled mass spectroscopy was performed both on the bulk and on the embedded material at 5°C.min^{-1}. Figure 4 clearly demonstrates that the decomposition path on bulk $Mg(BH_4)_2$ and the impregnated one are different. For the first one (blue line on figure 4), three distinct hydrogen releases are observed while for the second one (red line on figure 4), only one single dehydrogenation step can be seen.

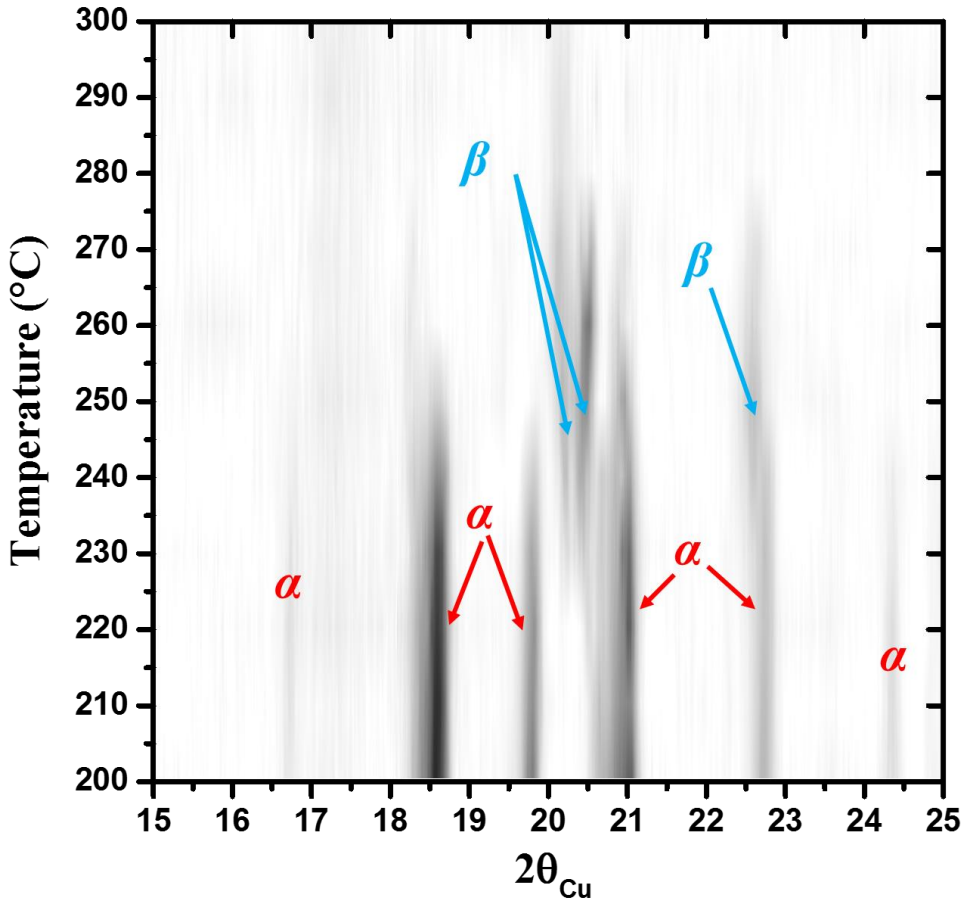

Figure 3. XRD diagrams upon heating up to 300°C for Ni-Pt@C impregnated with $Mg(BH_4)_2$. Blue arrows: β-$Mg(BH_4)_2$, red arrows: α-$Mg(BH_4)_2$.

If only the nano-confinement is used (no catalyst), we observe two steps in the dehydrogenation process (cf. Figure S3, black line). The first peak at 325°C is attributed to the decomposition of $Mg(BH_4)_2$ inside the carbon matrix and the second peak (375°C) to some magnesium borohydride outside the porosity which behaves as the bulk material. On the other hand, if only the catalyst is added to the borohydride, we observe three sharp peaks at 260°C, 350°C and 375°C (cf. Figure S3 blue line). We assume that the first and smallest one is due to the decomposition of $Mg(BH_4)_2$ in contact with the catalyst. The last two peaks clearly correspond to the normal decomposition of bulk $Mg(BH_4)_2$. The absence of a carbon support decreases significantly the efficiency of the catalytic nanoparticles. Thus, the concomitant effect of the nano-confinement and the addition of catalyst is beneficial for the desorption process and leads to a

single step decomposition at a lower temperature than that achieved with the addition of catalyst only or with the nano-confinement only (cf. Figure S3 red line).

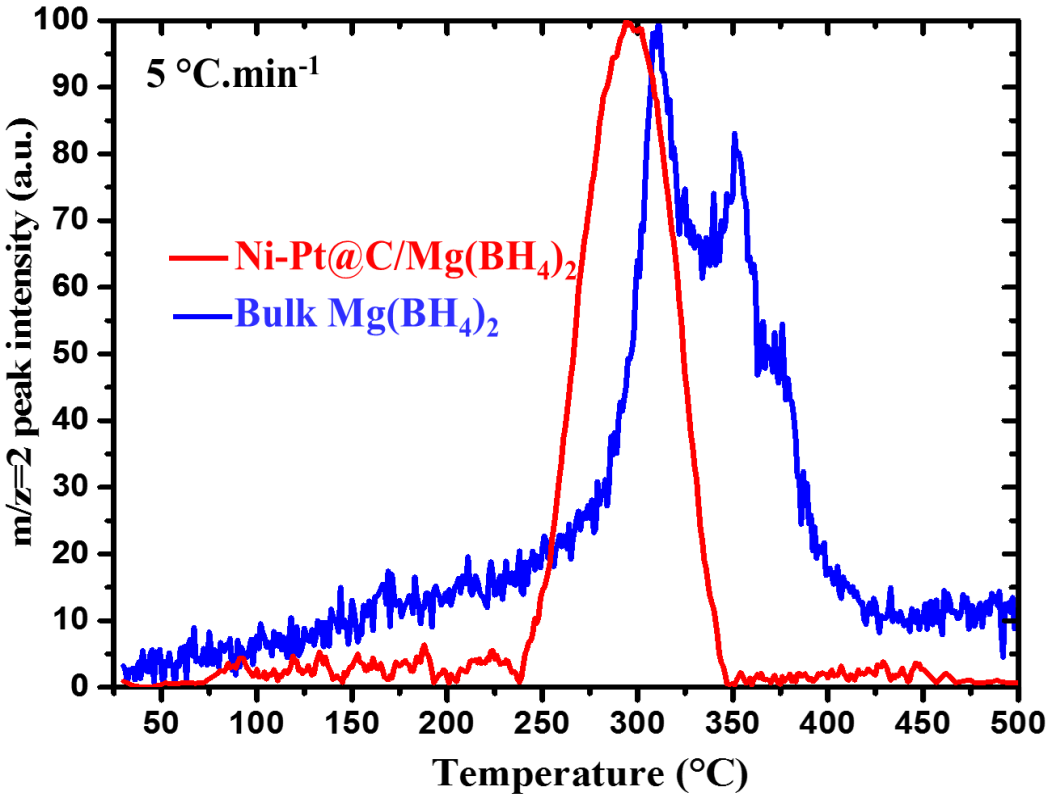

Figure 4. Temperature controlled mass spectroscopy for m/z=2 at 5°C.min^{-1} of Ni-Pt@C impregnated with $Mg(BH_4)_2$ (red line) and of bulk material (blue line)

3.4. Activation energy and performances of Ni-Pt@C+$Mg(BH_4)_2$

The activation energy of our sample was initially determined using the Kissinger equation (cf. Equation 1) from the DSC curves recorded at different heating rates and compared to that of bulk γ-$Mg(BH_4)_2$.

$$d\left(\ln \frac{\beta}{T^2}\right) / d\left(\frac{1}{T}\right) = \frac{-Ea}{R} \qquad \textbf{(Equation 1)}$$

with β : Heating rate (K.min^{-1})

T : Temperature of the peak maximum (K)

R : Gas constant ($J.mol^{-1}.K^{-1}$)

Ea : Activation energy ($J.mol^{-1}$)

The main problem for this analysis was the strong broadening of the endothermic peak resulting from both the nano-confinement and the change of decomposition path. Consequently, the Kissinger plot ($\ln \beta/T^2$ as a function of 1/T) showed a very poor linearity and the Kissinger equation limitations were not respected. Instead of using the DSC endothermic peak of decomposition, the peak recorded by mass spectroscopy for the H_2 release (m/z = 2) was used (cf. Figure 5). Since the hydrogen desorption is a first order reaction, the Kissinger approximation was fully respected in this case. Thanks to this method, we were able to determine the activation energy of the decomposition of our compound to 174 ± 14 $kJ.mol^{-1}$ of $Mg(BH_4)_2$, which is well below the value of 340 $kJ.mol^{-1}$ reported in the literature for bulk $Mg(BH_4)_2$ [28].

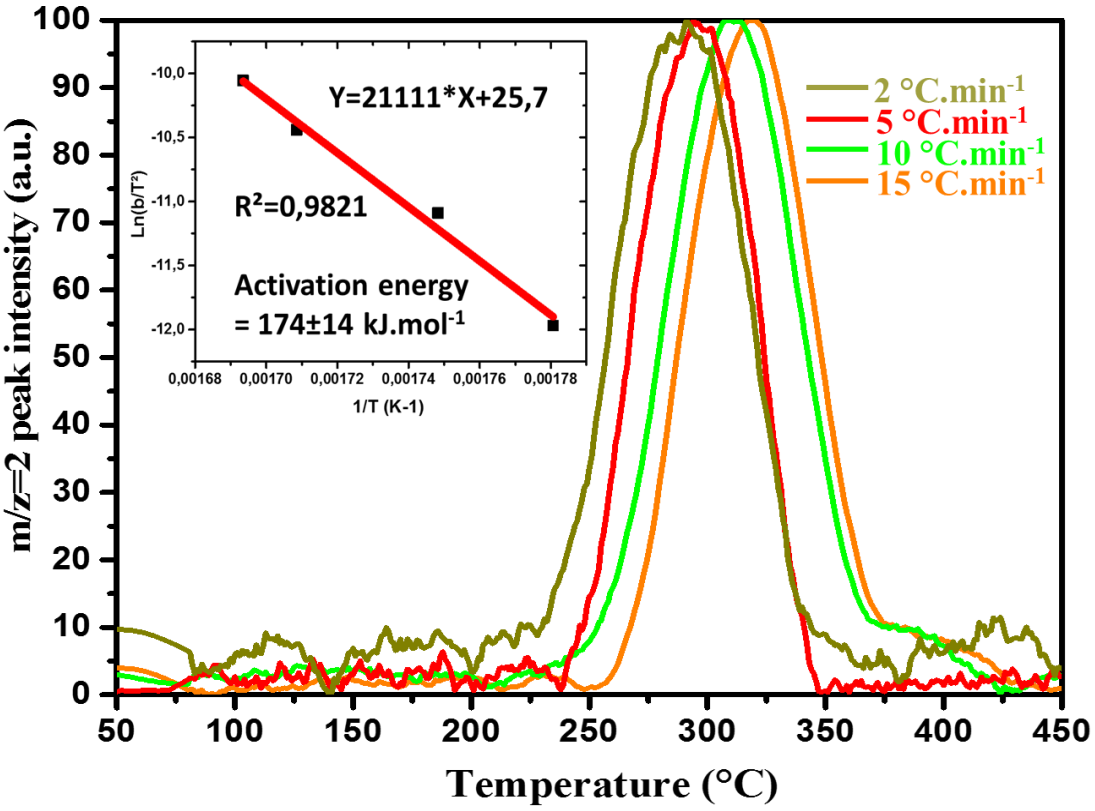

Figure 5. Curves of H_2 emission (m/z=2) recorded by mass spectroscopy at different heating rates for Ni-Pt@C impregnated with $Mg(BH_4)_2$. Insert: Kissinger plot allowing the calculation of the activation energy of the desorption process.

In a previous report [28] by Fichtner *et al.* on $Mg(BH_4)_2$ confined into mesoporous carbons, a decrease of the activation energy from 310.7 $kJ.mol^{-1}$ to 176.2 $kJ.mol^{-1}$ was determined. In our study, we determined an energy of 347 ± 17 $kJ.mol^{-1}$ for bulk $Mg(BH_4)_2$ and 262 ± 11 $kJ.mol^{-1}$ for $Mg(BH_4)_2$ confined into the mesoporous carbon without catalyst. Most interestingly, the decomposition of our sample occurs in only one step instead of three as usually reported, with a lower temperature of decomposition (250-350°C) due to the synergetic effects of Ni-Pt nanocatalysts and nano-confinement into a mesoporous carbon.

The quantity of hydrogen released by the Ni-Pt@C sample loaded with 30 wt.% of $Mg(BH_4)_2$ was measured by volumetric method. The theoretical hydrogen release is 4.5 wt.% taking into account the weights of carbon and Ni-Pt catalyst. The results here clearly demonstrate a full desorption at 400°C with the release of 8 hydrogen atoms per formula unit (cf. the red curve on Figure 6). The main hydrogen release occurs at 250°C in agreement with the XRD measurement done previously. Unfortunately, no rehydrogenation of the decomposition products from Ni-Pt@C + $Mg(BH_4)_2$ material was possible when a pressure of 100 bar was applied in a range of temperatures going from 50°C to 400°C. It is worth noting that this desorption capacity of 4.5 wt.% could be improved by using mesoporous carbons with a larger porous volume (up to 1 $cm^3.g^{-1}$ is feasible) allowing to get more active material, i.e. more $Mg(BH_4)_2$, in the final composite material.

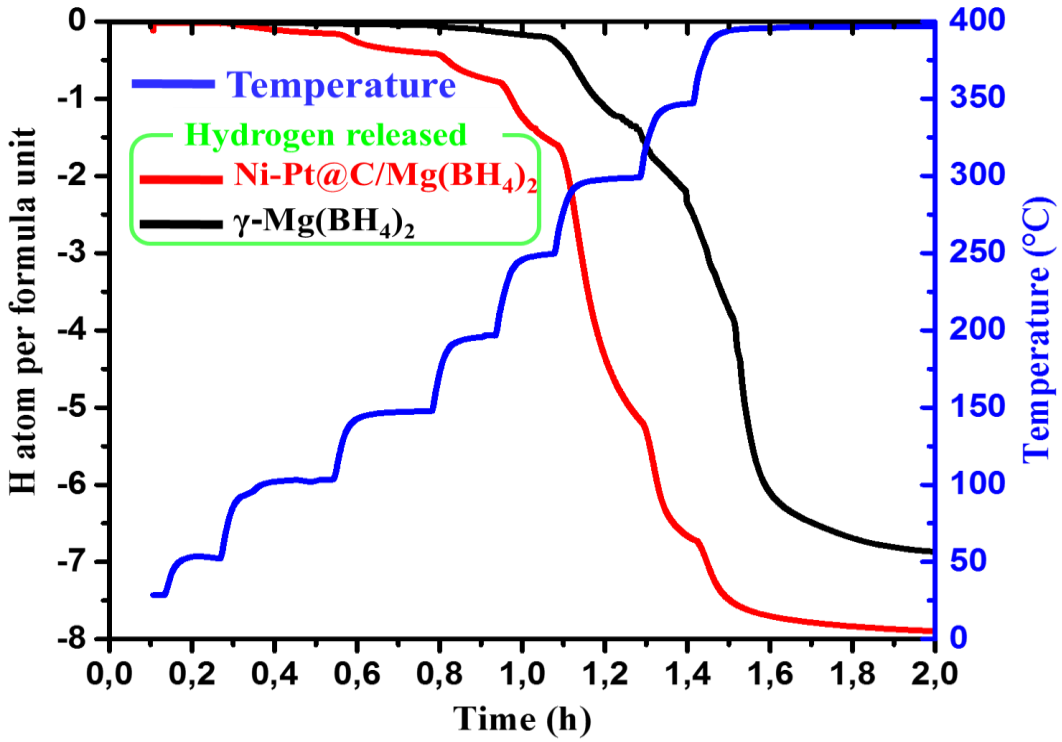

Figure 6. Hydrogen desorption measured by volumetric method, the red curve represents the number of H atoms desorbed by $Mg(BH_4)_2$ formula unit for the sample Ni-Pt@C+ $Mg(BH_4)_2$, the black curve represents bulk $Mg(BH_4)_2$ for comparison and the blue curve the temperature.

Considering the one-step decomposition, the full release of hydrogen and the absence of B_2H_6 generated during the decomposition, we suppose that only those two reactions can have occurred (reactions 4 and 5).

$$\alpha\text{-}Mg(BH_4)_2 \rightarrow \beta\text{-}Mg(BH_4)_2 \rightarrow MgB_2 + 4\ H_2 \quad (4)$$

$$\alpha\text{-}Mg(BH_4)_2 \rightarrow \beta\text{-}Mg(BH_4)_2 \rightarrow Mg + 2B + 4\ H_2 \quad (5)$$

In order to determine which reaction occurred, TEM and electron diffraction were performed on the sample desorbed at 400°C but only revealed the presence of MgO in the shape of flat platelets with a thickness of about 2-3 nm and diameters in the 5-10 nm range (cf. Figure S4 in the Supporting information). Our sample was heat treated on a PCT device in order to determine its hydrogen release performances (cf. Figure 6) without any contact with air or moisture but,

unfortunately, MgO was observed by TEM. It is worth mentioning that Mg and even MgB_2 are very sensitive to the oxidation at the nanoscale [46-48]. Nevertheless, this TEM observation was useful and confirmed that $Mg(BH_4)_2$ nucleated into the mesoporous carbon was at the nanoscale (below 10 nm in size) and that the thermal decomposition does not lead to the collapse of the carbon scaffold. Similarly, the size and the distribution of the Ni-Pt catalyst appear unaffected by the thermal treatment up to 400°C.

However, it is worth mentioning that some nanoparticles have reacted with boron forming Ni-B borides as demonstrated by EELS spectroscopy (cf. the spectrum at the top of Figure S5a in the Supporting information). The EELS spectrum recorded on these Ni-Pt particles after hydrogen desorption at 400°C has actually a shape very similar to those reported in the literature for Ni_2B or $Ni_{60}B_{40}$ materials (cf. Figure S5b). It appears therefore that, in spite of the presence of a Pt shell around the Ni particles cores, the formation of Ni-B borides can occur. This is not a disadvantage as the catalytic effect of Ni_2B is well known for hydrogenation reaction [49-50]. Thus, the catalytic species in our material is rather a mixture of Ni-B borides and Pt at the nanoscale.

4. Conclusions

We successfully applied both nano-confinement and catalysis to $Mg(BH_4)_2$ and investigated the effects on its decomposition pathway. More specifically, a mesoporous carbon (with a main pores size of 8 nm) was loaded with 5 wt.% of Ni-Pt core-shell nanoparticles acting as catalyst and then impregnated by $Mg(BH_4)_2$ leading to a final composite material containing 30 wt.% of $Mg(BH_4)_2$. The thermal desorption of the resulting composite material is different from bulk $Mg(BH_4)_2$ with a single step of hydrogen release making this decomposition pathway one of the most simple found in the literature for $Mg(BH_4)_2$. Interestingly, the hydrogen release is fully completed for our material, i.e. 8 H atoms per $Mg(BH_4)_2$ formula unit are released, in less than 2 hours at 350°C. The activation energy of the desorption process is much below that of the bulk material with a value of 178 ± 14 $kJ.mol^{-1}$ as determined by the Kissinger's method. The catalyst and confinement have a concomitant effect by improving the hydrogen release to a larger extent than that obtained by nano-confinement only or by catalysts addition only.

Acknowledgements

This work was financed by the European Fund for Economic and Regional Development (FEDER) and the regional council of Picardy. We are thankful to Matthieu Courty for his contribution to this work and his technical support for the thermal analyses of the samples.

References

[1] L. Schlapbach, A. Züttel, Hydrogen-storage materials for mobile applications, Nature 414 (2001) 353-358.

[2] I.P. Jain, Hydrogen the fuel for 21st century, Int. J. Hydrogen Energy. 34 (2009) 7368–7378.

[3] A.J. Bard, M.A.A. Fox, Artificial photosynthesis: Solar splitting of water to hydrogen and oxygen, Acc. Chem. Res. 28 (1995) 141–145.

[4] M.A. Green, K. Emery, Y. Hishikawa, W. Warta, E.D. Dunlop, Solar cell efficiency tables (Version 45), Prog. Photovoltaics Res. Appl. 23 (2015) 1–9.

[5] D. Mori, K. Hirose, Recent challenges of hydrogen storage technologies for fuel cell vehicles, Int. J. Hydrogen Energy 34 (2009) 4569–4574.

[6] J. Wolf, Liquid-hydrogen technology for vehicles, MRS Bull. 27 (2002) 684–687.

[7] S.M. Aceves, F. Espinosa-Loza, E. Ledesma-Orozco, T.O. Ross, A.H. Weisberg, T.C. Brunner, O. Kircher, High-density automotive hydrogen storage with cryogenic capable pressure vessels, Int. J. Hydrogen Energy 35 (2010) 1219-1226.

[8] Y. Nakamori, K. Miwa, A. Ninomiya, H. Li, N. Ohba, S.I. Towata, A. Züttel, S. Orimo, Correlation between thermodynamical stabilities of metal borohydrides and cation electronegativites: First-principles calculations and experiments, Phys. Rev. B 74 (2006) 045126.

[9] S. Orimo, Y. Nakamori, J.R. Eliseo, A. Züttel, C.M. Jensen, S. Orimo, Y. Nakamori, J.R. Eliseo, A. Züttel, C. M. Jensen, Complex hydrides for hydrogen storage, Chem. Rev. 107 (2007) 4111–4132.

[10] D.S. Marynick, W.N. Lipscomb, Crystal structure of beryllium borohydride, Inorg. Chem. 11 (1972) 820–823.

[11] K. Miwa, N. Ohba, S.I. Towata, Y. Nakamori, S. Orimo, First-principles study on lithium borohydride $LiBH_4$, Phys. Rev. B 69 (2004) 245120.

[12] M. Au, A. Jurgensen, Modified lithium borohydrides for reversible hydrogen storage modified lithium borohydrides for reversible hydrogen storage, J. Phys. Chem. B 110 (2006) 7062–7067.

[13] S. Aldridge, A.J. Blake, A.J. Downs, R.O. Gould, S. Parsons, C.R. Pulham, Some tetrahydroborate derivatives of aluminium: Crystal structures of dimethylaluminium tetrahydroborate and the α and β phases of aluminium tris(tetrahydroborate) at low temperature, J. Chem. Soc. - Dalt. Trans. 0 (1997) 1007–1012.

[14] H.W. Li, Y. Yan, S.I. Orimo, A. Züttel, C.M. Jensen, Recent progress in metal borohydrides for hydrogen storage, Energies 4 (2011) 185–214.

[15] Y. Liu, Y. Yang, M. Gao, H. Pan, Tailoring thermodynamics and kinetics for hydrogen storage in complex hydrides towards applications, Chem. Record 16 (2016) 189–204.

[16] Y. Filinchuk, B. Richter, T.R. Jensen, V. Dmitriev, D. Chernyshov, H. Hagemann, Porous and dense magnesium borohydride frameworks: Synthesis, stability, and reversible absorption of guest species, Angew. Chemie - Int. Ed. 50 (2011) 11162–11166.

[17] M.J. Qin, X.L. Wang, S. Soltanian, A.H. Li, H.K. Liu, S.X. Dou, Dependence of the flux-creep activation energy on current density and magnetic field for the (formula presented) superconductor, Phys. Rev. B 64 (2001) 060505.

[18] A.A. Ibikunle, A.J. Goudy, Kinetics and modeling study of a $Mg(BH_4)_2/Ca(BH_4)_2$ destabilized system, Int. J. Hydrogen Energy 37 (2012) 12420–12424.

[19] B. Dai, D.S. Sholl, J.K. Johnson, First-principles study of experimental and hypothetical $Mg(BH_4)_2$ crystal structures, J. Phys. Chem. C 112 (2008) 4391–4395.

[20] M.J. Van Setten, G.A. De Wijs, M. Fichtner, G. Brocks, A density functional study of α-$Mg(BH_4)_2$, Chem. Mater. 20 (2008) 4952–4956.

[21] M.D. Riktor, M.H. Sørby, K. Chłopek, M. Fichtner, F. Buchter, A. Züttel, B.C. Hauback, In situ synchrotron diffraction studies of phase transitions and thermal decomposition of $Mg(BH_4)_2$ and $Ca(BH_4)_2$, J. Mater. Chem. 17 (2007) 4939-4942.

[22] C.J. Sahle, S. Kujawski, A. Remhof, Y. Yan, N.P. Stadie, A. Al-Zein, M. Tolan, S. Huotari, M. Krisch, C. Sternemann, In situ characterization of the decomposition behavior of $Mg(BH_4)_2$ by X-ray Raman scattering spectroscopy, Phys. Chem. Chem. Phys. 18 (2016) 5397–5403.

[23] N. Hanada, K. Chłopek, C. Frommen, W. Lohstroh, M. Fichtner, Thermal decomposition of $Mg(BH_4)_2$ under He flow and H_2 pressure, J. Mater. Chem. 18 (2008) 2611-2614.

[24] V.N. Konoplev, V.M. Bakulina, Some properties of magnesium borohydride, Bull. Acad. Sci. USSR Div. Chem. Sci. 20 (1971) 136–138.

[25] F. Buchter, T. Matsunaga, P. Mauron, Y. Nakamori, S.-I. Orimo, M. Bielmann, N. Ohba, K. Miwa, A. Züttel, S. Towata, F. Buchter, P. Mauron, M. Bielman, Y. Nakamori, S. Orimo, N. Ohba, K. Miwa, S. Towata, A. Züttel, Hydrogen storage properties of $Mg(BH_4)_2$, J. Alloys Compd. 459 (2008) 583–588.

[26] O. Zavorotynska, A. El-Kharbachi, S. Deledda, B.C. Hauback, Recent progress in

magnesium borohydride $Mg(BH_4)_2$: Fundamentals and applications for energy storage, Int. J. Hydrogen Energy 41 (2016) 14387–14403.

[27] B. Sakintuna, F. Lamari-Darkrim, M. Hirscher, Metal hydride materials for solid hydrogen storage: A review, Int. J. Hydrogen Energy 32 (2007) 1121–1140.

[28] M. Fichtner, Z. Zhao-Karger, J. Hu, A. Roth, P. Weidler, The kinetic properties of $Mg(BH_4)_2$ infiltrated in activated carbon, Nanotechnology 20 (2009) 204029.

[29] R.J. Newhouse, V. Stavila, S.-J.J. Hwang, L.E. Klebanoff, J.Z. Zhang, Reversibility and improved hydrogen release of magnesium borohydride, J. Phys. Chem. C 114 (2010) 5224–5232.

[30] M. Rueda, L.M. Sanz-Moral, A. Girella, P. Cofrancesco, C. Milanese, Ï. Martïn, Á. Martín, Reversible hydrogen sorption in the composite made of magnesium borohydride and silica aerogel, Int. J. Hydrogen Energy 41 (2016) 15245–15253.

[31] Y. Liu, Y. Yang, Y. Zhou, Y. Zhang, M. Gao, H. Pan, Hydrogen storage properties and mechanisms of the $Mg(BH_4)_2$–$NaAlH_4$ system, Int. J. Hydrogen Energy. 37 (2012) 17137–17145

[32] Y. Yang, M. Gao, Y. Liu, J. Wang, J. Gu, H. Pan, Z. Guo, Multi-hydride systems with enhanced hydrogen storage properties derived from $Mg(BH_4)_2$ and $LiAlH_4$, Int. J. Hydrogen Energy. 37 (2012) 10733–10742.

[33] M.A. Wahab, Y. Jia, D. Yang, H. Zhao, X. Yao, Enhanced hydrogen desorption from $Mg(BH_4)_2$ by combining nanoconfinement and a Ni catalyst, J. Mater. Chem. A 1 (2013) 3471-3478.

[34] M.A. Wahab, D.J. Young, A. Karim, S. Fawzia, J.N. Beltramini, Low-temperature hydrogen desorption from $Mg(BH_4)_2$ catalysed by ultrafine Ni nanoparticles in a mesoporous carbon matrix, Int. J. Hydrogen Energy 41 (2016) 20573–20582.

[35] S. Cahen, J.-B.B. Eymery, R. Janot, J.-M.M. Tarascon, Improvement of the $LiBH_4$ hydrogen desorption by inclusion into mesoporous carbons, J. Power Sources 189 (2009) 902–908.

[36] N. Brun, R. Janot, C. Sanchez, H. Deleuze, C. Gervais, M. Morcrette, R. Backov, Preparation of $LiBH_4$@carbon micro-macrocellular foams: Tuning hydrogen release through varying microporosity, Energy Environ. Sci. 3 (2010) 824–830.

[37] M. Depardieu, R. Janot, C. Sanchez, H. Deleuze, C. Gervais, M. Birot, M. Morcrette, R. Backov, Nano-spots induced break of the chemical inertness of boron: a new route toward reversible hydrogen storage applications, J. Mater. Chem. A 2 (2014) 7694–7701.

[38] D. Clémençon, J.F. Petit, U.B. Demirci, Q. Xu, P. Miele, Nickel- and platinum-containing core@shell catalysts for hydrogen generation of aqueous hydrazine borane, J. Power Sources 260 (2014) 77–81.

[39] Y. Chen, F. Yang, Y. Dai, W. Wang, S. Chen, Ni@Pt core−shell nanoparticles: Synthesis, structural and electrochemical properties, J. Phys. Chem. C 112 (2008) 1645–1649.

[40] P.L. Potapov, S.E. Kulkova, D. Schryvers, J. Verbeeck, Structural and chemical effects on

EELS L3,2 ionization edges in Ni-based intermetallic compounds, Phys. Rev. B 64 (2001) 184110.

[41] P. Ewels, T. Sikora, V. Serin, C.P. Ewels, L. Lajaunie, A complete overhaul of the Electron Energy-Loss Spectroscopy and X-Ray absorption spectroscopy database: eelsdb.eu, Microsc. Microanal. 22 (2016) 717–724.

[42] J.G. Railsback, A.C. Johnston-Peck, J. Wang, J.B. Tracy, Size-dependent nanoscale Kirkendall effect during the oxidation of nickel nanoparticles, ACS Nano. 4 (2010) 1913–1920.

[43] Y. Filinchuk, R. Černý, H. Hagemann, Insight into $Mg(BH_4)_2$ with synchrotron X-ray diffraction: Structure revision, crystal chemistry, and anomalous thermal expansion, Chem. Mater. 21 (2009) 925–933.

[44] W. David, S.K. Callear, M.O. Jones, P.C. Aeberhard, S.D. Culligan, A.H. Pohl, S.R. Johnson, K.R. Ryan, J.E. Parker, P.P. Edwards, C.J. Nuttall, A. Amieiro-Fonseca, The structure, thermal properties and phase transformations of the cubic polymorph of magnesium tetrahydroborate, Phys. Chem. Chem. Phys. 14 (2012) 11800–11807.

[45] J.-H.H. Her, P.W. Stephens, Y. Gao, G.L. Soloveichik, J. Rijssenbeek, M. Andrus, J.-C.C. Zhao, Structure of unsolvated magnesium borohydride $Mg(BH_4)_2$, Acta Crystallogr. Sect. B Struct. Sci. 63 (2007) 561–568.

[46] Z.Y. Fan, D.G. Hinks, N. Newman, J.M. Rowell, Experimental study of MgB_2 decomposition, Appl. Phys. Lett. 79 (2001) 87–89.

[47] D. Yang, H. Sun, H. Lu, Y. Guo, X. Li, X. Hu, Experimental study on the oxidation of MgB_2 in air at high temperature, Supercond. Sci. Technol. 16 (2003) 576–581.

[48] M.A. Imam, R.G. Reddy, Thermogravimetric analysis of simultaneous decomposition and formation of MgB_2, Miner. Met. Mater. Soc., Magnesium technology (2018) 173–179.

[49] R. Paul, P. Buisson, N. Joseph, Catalytic activity of nickel borides, Indus. Engineer. Chem. 44 (1952) 1006-1010.

[50] J. Nagy, I. Bodart-Ravet, E. Derouane, Preparation, characterization and catalytic activity of monodisperse colloidal metal boride, Faraday Discuss. Chem. Soc. 87 (1989) 189-198.

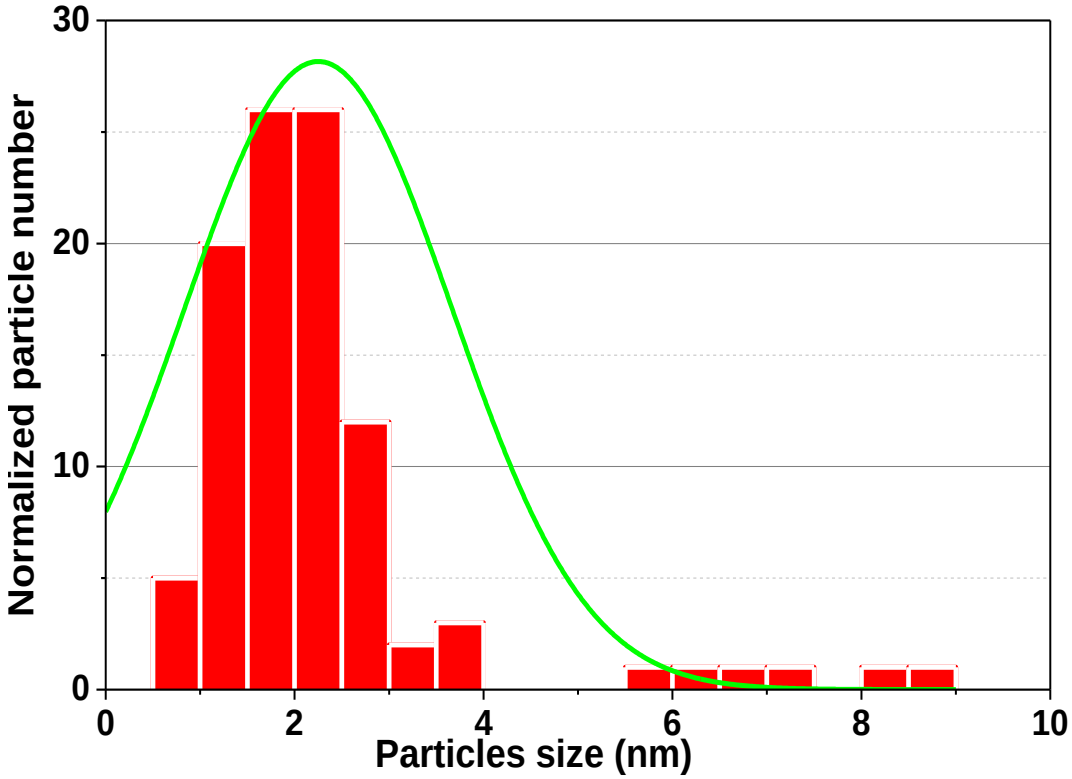

Figure S1. Size distribution of the Ni-Pt nanoparticles by statistic on HAADF-STEM images.

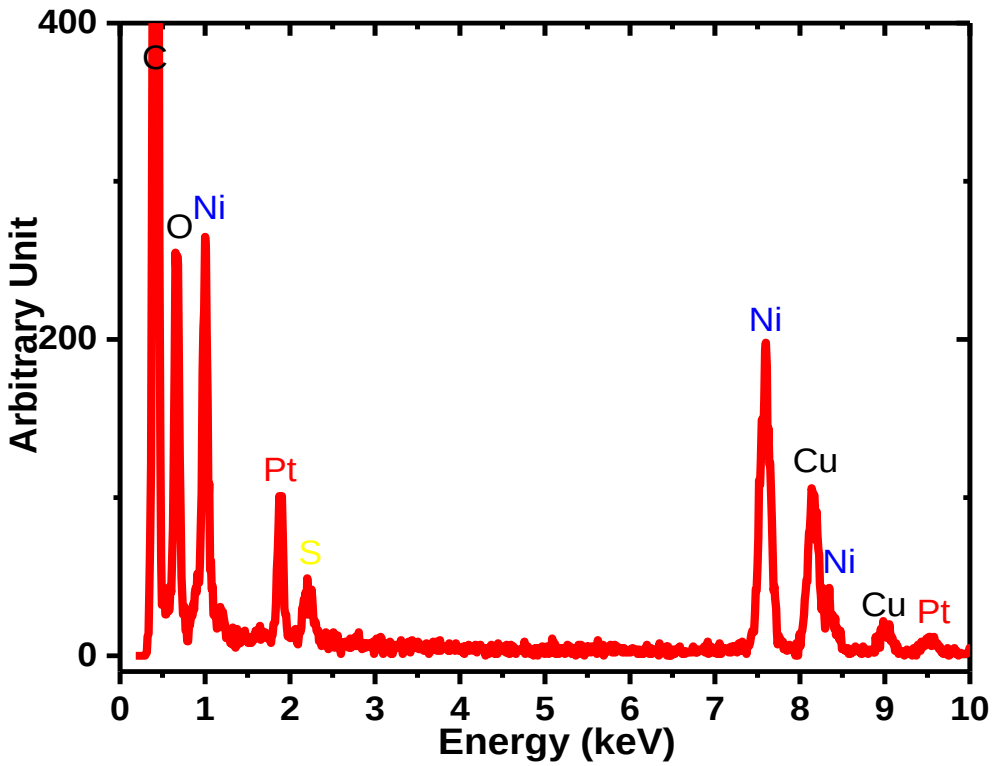

Element	% mass	Error (%)
Ni	90	±2
Pt	10	±2

Figure S2. EDS spectrum of the Ni-Pt@C particles. The detection of Cu is due to the use of a TEM copper grid.

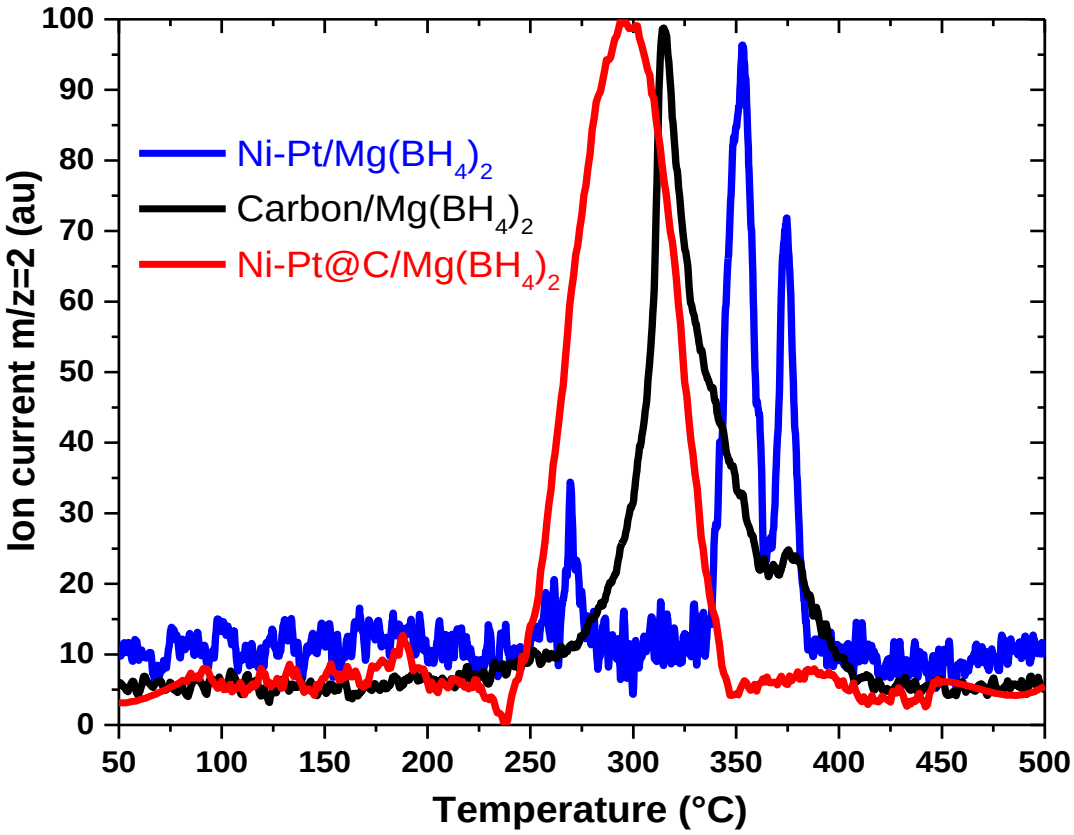

Figure S3. Curves of H_2 emission (m/z=2) recorded by mass spectroscopy at 5°C.min^{-1} for Ni-Pt@C impregnated with $Mg(BH_4)_2$ (in red), for $Mg(BH_4)_2$ solely nucleated into the mesoporous carbon (in black) and $Mg(BH_4)_2$ mixed with the Ni-Pt catalyst (in blue).

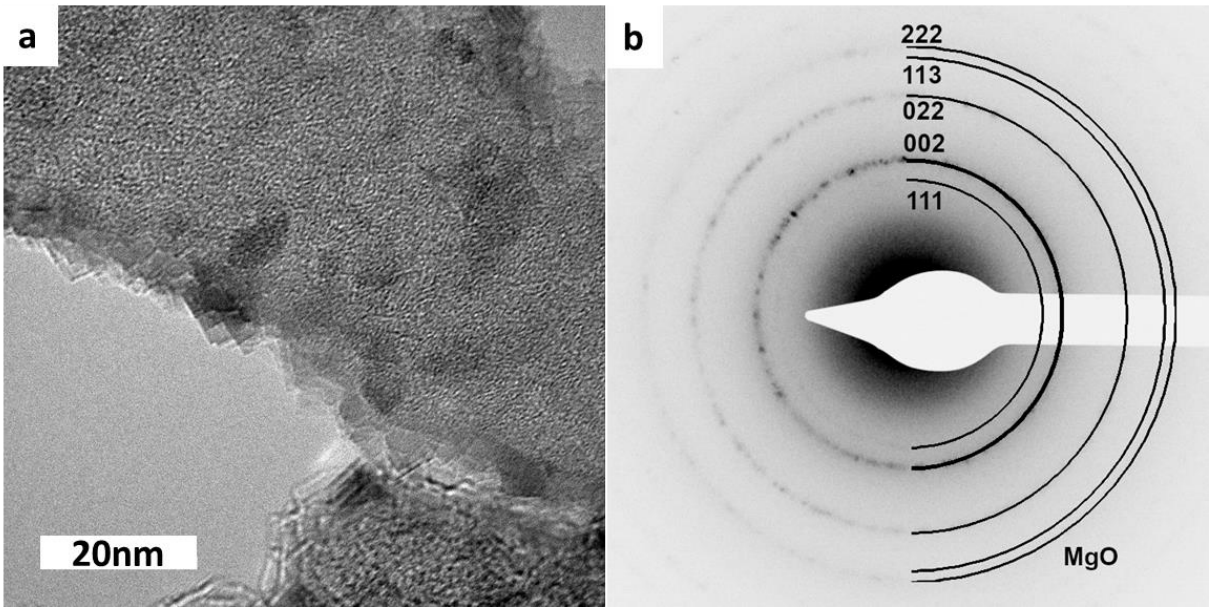

Figure S4. (**a)** TEM image of the sample $Mg(BH_4)_2$/Ni-Pt@C after dehydrogenation at 400°C, **(b)** Corresponding selected area electron diffraction (SAED) pattern corresponding to MgO.

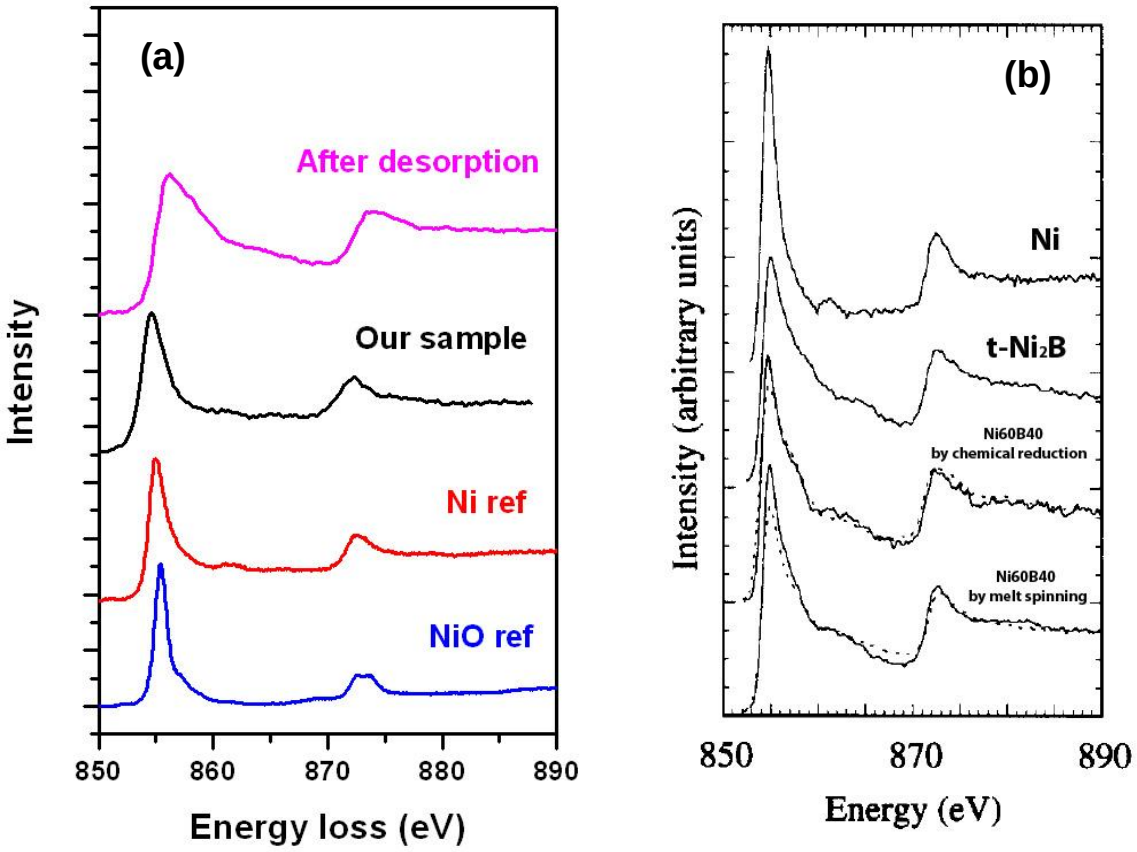

Figure S5. (a) EELS spectra at the Ni-L2,3 edge for our Ni-Pt@C + $Mg(BH_4)_2$ sample (in black) and the same after hydrogen desorption at 400°C (in pink). Ni in red and NiO in blue are used as references. (**b)** EELS spectra at the Ni-L2,3 edge for Ni and various Ni-B borides adapted from Reference: *G. Mountjoy, A. Corrias, P.H. Gaskell, J. Non-Crystalline Solids 192 (1995) 616-619.*